

Structure-sensitive Multi-scale Deep Neural Network for Low-Dose CT Denoising

Chenyu You, Qingsong Yang, Hongming Shan, Lars Gjestebj, Li Guang, Shenghong Ju, Zhuibang Zhang, Zhen Zhao, Yi Zhang, *Member, IEEE*, Wenxiang Cong, and Ge Wang*, *Fellow, IEEE*

Abstract—Computed tomography (CT) is a popular medical imaging modality in clinical applications. At the same time, the x-ray radiation dose associated with CT scans raises public concerns due to its potential risks to the patients. Over the past years, major efforts have been dedicated to the development of Low-Dose CT (LDCT) methods. However, the radiation dose reduction compromises the signal-to-noise ratio (SNR), leading to strong noise and artifacts that down-grade CT image quality. In this paper, we propose a novel 3D noise reduction method, called Structure-sensitive Multi-scale Generative Adversarial Net (SMGAN), to improve the LDCT image quality. Specifically, we incorporate three-dimensional (3D) volumetric information to improve the image quality. Also, different loss functions for training denoising models are investigated. Experiments show that the proposed method can effectively preserve structural and texture information from normal-dose CT (NDCT) images, and significantly suppress noise and artifacts. Qualitative visual assessments by three experienced radiologists demonstrate that the proposed method retrieves more detailed information, and outperforms competing methods.

Index Terms—Machine Learning, Low dose CT, Image denoising, Deep learning, Loss Function

I. INTRODUCTION

X-RAY computed tomography (CT) is one of the most used imaging modalities in various clinical, industrial, and other applications [1]. Nevertheless, the high risk of ionizing radiation associated with CT scans causes many patients to be concerned [2]. Studies from the National Council on Radiation Protection and Measurements (NCRP) demonstrate a 600% increase in medical radiation dose to the US population from 1980 to 2006, potentially increasing the future health risks to patients [3].

The main drawback of dose reduction is to increase the clinically unacceptable image background noise, which severely compromises diagnostic information. How to lower the exposure to ionizing radiation while maintaining high-quality

context features in low-dose CT (LDCT) images has been a longstanding challenge for researchers to explore under the well-known guiding strategy of ALARA (as low as reasonably achievable) [1].

Numerous methods have been designed for noise reduction in LDCT. These methods can be categorized as follows: (1) *Sinogram filtering-based techniques* [4]–[8]: these methods directly process projection data in the projection domain [6], bowtie filtering [7], and structural adaptive filtering [8]. The main advantage of these methods is computational efficiency. However, they may result in loss of structural information and spatial resolution in LDCT acquisition [6]–[8]; (2) *Iterative reconstruction (IR)* [9]–[18]: IR techniques may potentially produce high signal-to-noise ratio (SNR). However, these methods require substantial computational resource, optimal parameter settings and accurate modeling of noise properties; (3) *Image space denoising techniques* [18]–[23]: these techniques can be performed directly on reconstructed images so that they can be applied across various CT scanners at a very low cost. Examples are non-local means-based filters [14], [19], dictionary-learning-based K-singular value decomposition (K-SVD) method [18] and the block-matching 3D (BM3D) algorithms [22], [23]. Even though these algorithms greatly suppress noise and artifacts, edge blurring or loss of spatial resolution may still remain in the processed LDCT images.

Deep learning (DL) has received a tremendous amount of attention in the field of medical imaging [24], [25], such as brain image segmentation [26], image registration [27], [28], and medical image classification [29]. Recent studies demonstrate that deep learning (DL) techniques have yielded successful results for noise reduction in LDCT [30]–[35]. For example, Chen *et al.* [31] proposed a pioneering Residual Encoder-Decoder convolutional neural network (REN-CNN) to predict NDCT images from noisy LDCT images. This method greatly reduces the background noise and artifacts. However, the major limitation is that the content of the results is blurry since the method is iteratively minimizing the mean-squared error per voxel between generated LDCT and the corresponding NDCT images. To cope with this limitation, generative adversarial networks (GANs) [36] provide a feasible solution. The generator G learns to capture a real data distribution P_r and the discriminator D attempts to discriminate between the synthetic data distribution and the real data distribution. Note that the loss used in GAN, called adversarial loss, measures the distance between the synthetic data distribution and the real data distribution in order to improve the performance of G and D . Here the GAN uses

Asterisk indicates corresponding author.

C. You is with Departments of Bioengineering and Electrical Engineering, Stanford University, Stanford, CA, 94305 (e-mail: unicy@stanford.edu)

Q. Yang, H. Shan, L. Gjestebj, L. Guang, W. Cong, and G. Wang* are with Department of Biomedical Engineering, Rensselaer Polytechnic Institute, Troy, NY, 12180 (e-mail: yangq4@rpi.edu, shanh@rpi.edu, gjestl@rpi.edu, lig10@rpi.edu, congw@rpi.edu, wangg6@rpi.edu)

S. Ju, Z. Zhao are with Jiangsu Key Laboratory of Molecular and Functional Imaging, Department of Radiology, Zhongda Hospital, Medical School, Southeast University, Nanjing 210009, China (e-mail: jsh0836@hotmail.com, zhaozhen8810@126.com)

Y. Zhang is with the College of Computer Science, Sichuan University, Chengdu 610065, China (e-mail: yzhang@scu.edu.cn)

Z. Zhang is with Department of Radiology, Wuxi No.2 People's Hospital, Wuxi, 214000, China (e-mail: zhangzhuibang@163.com)

Jensen-Shannon (JS) divergence to evaluate the similarity of the two data distributions [36]. However, several problems still exist in training GAN, such as unstable training or non-convergence issues. To cope with these issues, Arjovsky *et al.* introduced the Wasserstein distance instead of Jensen-Shannon divergence to improve the stability of the neural network training [37]. We discuss more details in Section II-D3.

Our previous work [33], which first introduced perceptual loss to capture perceptual differences between denoised LDCT images and the reference NDCT images, provides the perceptually better results for clinical diagnosis but yields low scores in image quality metrics. Since image quality assessment metrics to some extent evaluate the generated images with reference to the gold-standard over local textures in the images, optimizing perceptual loss to satisfy perceptual requirements does not ensure results with accurate anatomical information. To further address the issues mentioned above and inspired by remarkable success for noise-reduction in [32], [38], in this paper, we proposed a novel 3D clinical Structure-sensitive Multi-scale Generative Adversarial Net (SMGAN) to capture more subtle local structural features while maintaining high visual sensitivity. The proposed structure-sensitive loss leverages a mixture of adversarial loss [37], perceptually-favorable structural loss and pixel-wise L_1 loss. Moreover, to better validate the clinical image quality processed by our proposed method, we performed qualitative image assessments by three expert radiologists. Last but not least, we also investigate the feasibility and accuracy of mapping the noisy LDCT images to true data distributions in the space of real NDCT images through the WGAN framework.

Our main contributions and innovations in this paper are summarized below:

- 1) To better render the underlying structural information between LDCT and NDCT images, we adopt a 3D CNN model as a generator based on WGAN which can integrate spatial information to enhance the image quality and yield 3D volumetric results for better diagnosis.
- 2) To consider the structural and perceptual difference between generated LDCT images and gold-standard, structure-sensitive loss can enhance the accuracy and robustness of the algorithm. Different from [33], we replace perceptual loss with the combination of L_1 loss and structural loss to capture local anatomical structures while reducing background noise.
- 3) To better compare the performance of the 2D and the 3D models, we perform extensive investigations and evaluations on their convergence rate and denoising performance.

This paper is organized as follows: Section II introduces the proposed methods and analyzes the impact of each loss function on clinical image quality. The experimental settings and results are presented in Section III, and Section IV discusses our proposed methods. Finally, the concluding summary of our proposed methods and future plans are drawn in Section V.

II. METHODS

A. Overview

Assuming that $\mathbf{y} \in \mathbb{R}^{H \times W \times D}$ denotes the original LDCT image, and $\mathbf{x} \in \mathbb{R}^{H \times W \times D}$ denotes the corresponding NDCT image, the relationship can be expressed as:

$$\mathbf{y} = T(\mathbf{x}) + \epsilon \quad (1)$$

where $T : \mathbb{R}^{H \times W \times D} \rightarrow \mathbb{R}^{H \times W \times D}$ is a generic noising process that degrades the real sample \mathbf{x} of NDCT to a corresponding LDCT sample \mathbf{y} in a non-linear way. ϵ stands for the additive noise and unmodeled dynamics, and H , W , D are height, width, and depth, respectively.

From another standpoint, considering that the real NDCT distribution P_r is unknown, we focus on extracting information to recover desired synthetic images \mathbf{x} from the noisy LDCT images \mathbf{y} . In general, the noise distribution in CT images is regarded as the mixture of Poisson quantum noise and Gaussian electronic noise [39]. Compared with traditional denoising methods, the DL-based method is capable of effectively modeling any type of data distributions since the DL-based denoising model itself can easily derive the variational noise model that features the statistical properties of mixed noise distributions. Therefore, the proposed DL-based denoising network is to solve the inverse problem $T^\dagger \approx T^{-1}$ to retrieve feasible images $\hat{\mathbf{x}}$, and the inverse problem can be expressed as:

$$T^\dagger \mathbf{y} = \hat{\mathbf{x}} \approx \mathbf{x} \quad (2)$$

As shown in Fig.1, the overall network constitutes three parts. Part 1 is the generator G , part 2 is the structure-Sensitive loss (SSL) function, and part 3 is the discriminator D . G maps a volumetric LDCT image to the NDCT feature space, thereby yielding an estimated NDCT image. The SSL function computes the structure-sensitive dissimilarity which encodes multi-scale structural information. The loss computed by the SSL function aims to improve the ability of G to generate more realistic results. D distinguishes a pair of synthetic LDCT images and real NDCT images based on the anatomical details. If D can quickly identify the input image as "synthetic" or "real" correctly and tell us the discrepancy between the estimated CT image and the corresponding real NDCT image, it means that G does not yield the high-quality estimation results; thus, G needs to optimize its performance to generate better results. Otherwise, D needs to upgrade its ability. Hence, G and D are in a zero-sum game: G attempts to generate a convincing estimate of NDCT image while D aims to distinguish the estimated image from real NDCT images. See Sections II-C and II-D for more details about network structure and loss functions.

B. 3D Spatial Information

The advantages of using 3D spatial information are as follows. First, volume imaging and 3D image display have become routine standards for radiologists' daily diagnostics since they offer both radiologists' and patients volume visualization to benefit clinical practice [40]. So, there is a large amount of 3D NDCT and LDCT data available in real life, but most of

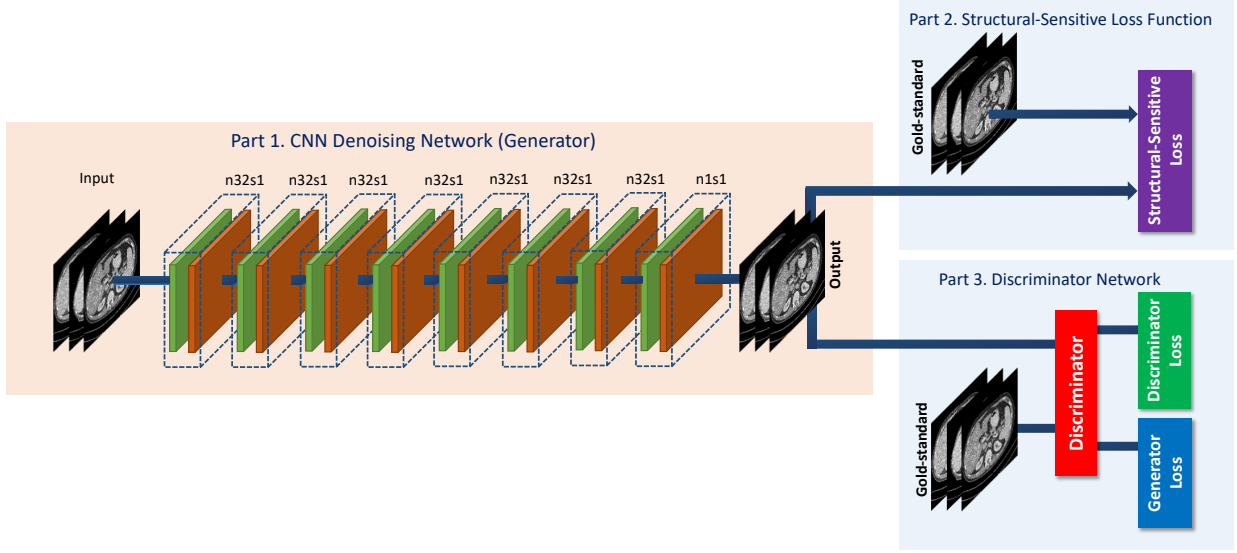


Fig. 1: The overall structure of the proposed SMGAN network. Note that the variable n denotes the number of filters and s denotes the stride size.

the networks adopt a 2D-based architecture. Last but not least, the adjacent cross-section slices from 3D CT images exhibit strong spatial correlations that can preserve more information in sagittal and coronal directions than 2D-based models.

As mentioned above, we propose a 3D ConvNet as the generator and a 3D structure-Sensitive loss (SSL) function in this paper. In addition, we extract expanded 3D image patches and use a 3D filter instead of a 2D filter. The generator in our network takes 3D volumetric LDCT patches as the input and trains them across 3D non-linear transform operations. The details of the network architecture are discussed in the following Section II-C.

Please note that our 2D denoising network is referred as SMGAN-2D and our 3D denoising network is referred as SMGAN-3D.

C. Network Structure

Inspired by the studies in [32], [33], here we introduce our proposed SMGAN-3D network structure in detail. First, in Section II-C1, we present the 3D generator G which captures local anatomical details through the neural network for better estimation. Then, the 3D SSL function which guides the network's learning is presented in Section II-C2. Finally, we outline the structure of the 2.5D discriminator D which distinguishes between two images in Section II-C3.

1) **3D CNN Generator:** The generator G consists of eight 3D convolutional (Conv) layers. The first 7 layers each have 32 filters and the last layer has only 1 filter. Based on our practical experience, the odd-numbered convolutional layers have $3 \times 3 \times 1$ filters, and the even-numbered convolutional layers have $3 \times 3 \times 3$ filters. The size of the extracted 3D patches used as the input is $80 \times 80 \times 11$. See Fig. 1. Note that the variable n denotes the number of the filters and s denotes the stride size which means the step size of the filter when moving across the image so that $n32s1$ stands

for 32 feature maps with stride one pixel. Furthermore, a pooling layer after each Conv layer may lead to loss of subtle textural and structural information, and spatial inconsistency in training stages. Therefore, the pooling layer is not applied in this network. Next, the Rectified Linear Unit (ReLU) [41] is utilized as the activation function after each Conv layer. The benefits to utilize ReLU are as follows. First, it produces non-linear interactions with its input, which in turn prevents the generated results from being equal to a linear transformation of the input. Second, it is crucial to maintain the sparsity in the inputs to each Conv layer to perform effective feature extraction in high-dimensional feature space.

2) **Structure-Sensitive Loss (SSL) Function:** The proposed 3D SSL function measures the patch-wise error between the 3D output from 3D ConvNet and the 3D NDCT images in spatial domain. This error was back-propagated [42] through the neural network to update the weights of network. See Section II-D for more details about loss functions which are embedded in the proposed function.

3) **Discriminator:** The discriminator D used in this network is made up of six convolutional layers with 64, 64, 128, 128, 256, and 256 filters and the kernel size of 3×3 . Two fully-connected (FC) layers produce 1024 and 1 feature maps respectively. Each layer is followed by a leaky ReLU in the manner of $\max(0, x) - \alpha \max(0, -x)$ [41] where α is a small constant. A stride of one pixel is applied for odd-numbered Conv layers and a stride of two pixels for even-numbered Conv layers. The input fed to D has the size of $64 \times 64 \times 3$, and is the output of G . The reason why we use a 2D filter in D is to lower the computational complexity. Since the adversarial loss between each two adjacent layers in one volumetric patch contribute equally to the weighted average in one iteration, it adds no computational expense and also takes into account spatial correlations. Following the suggestion in [37], we removes the sigmoid cross entropy layer in D .

D. Loss Functions for Noise Reduction

In this section, since the loss function is considered as the guider in training the neural network, we explore and evaluate the impact of different loss functions on noise reduction for LDCT. Next, we propose to utilize mixed loss functions to encourage high diagnostic quality of generated images.

1) **L_2 loss**: The L_2 loss can efficiently suppress the background noise, but it makes the denoised results unnatural and blurs the image contents. This is expected due to its regression-to-mean nature [38], [43]. Furthermore, L_2 loss assumes that background noise is white Gaussian noise, which is independent of local image features [44]. However, the noise within the CT system comes from various sources, such as quantum noise. This is another reason why the diagnostic image quality optimized by L_2 loss is undesirable.

The formula of L_2 loss is expressed as:

$$L_2 = \frac{1}{HWD} \|G(\mathbf{y}) - \mathbf{x}\|_2^2 \quad (3)$$

where H , W , D stand for the height, width, and depth of the 3D image patches, respectively, \mathbf{x} denotes gold-standard images (NDCT), and $G(\mathbf{y})$ represents the generated images from source (LDCT) images \mathbf{y} . It is worth noting that since L_2 loss has appealing properties of differentiability, convexity, and symmetry, the mean squared error (MSE) or L_2 loss is still a popular choice in denoising tasks [45].

2) **L_1 loss**: Even if L_1 loss and L_2 loss are both the mean-based loss function, the impacts of these two loss functions on denoising are different. Compared with L_2 loss, L_1 loss does not over-penalize large differences or tolerate small errors between denoised images and gold-standard images. Thus, L_1 loss can alleviate some limitations of L_2 loss we mentioned above. Additionally, L_1 loss enjoys the same fine characteristics as L_2 loss, like a fast convergence speed.

The formula of L_1 loss is expressed as:

$$L_1 = \frac{1}{HWD} |G(\mathbf{y}) - \mathbf{x}| \quad (4)$$

As shown in Fig. 3-6, compared with L_2 loss, L_1 loss reduces over-blurring effects, though a blocky effect remains. Further discussion about these results is presented in Section III.

3) **Adversarial loss**: The improved Wasserstein distance with the regularization term proposed in [43] is expressed as:

$$L_{adv} = -\mathbb{E}[D(\mathbf{x})] + \mathbb{E}[D(\mathbf{z})] + \lambda \mathbb{E}[(\|\nabla_{\hat{\mathbf{x}}} D(\hat{\mathbf{x}})\|_2 - 1)^2] \quad (5)$$

where the first two terms are computed for Wasserstein distance and the third term is the gradient penalty term. It is worth noting that \mathbf{z} denotes $G(\mathbf{y})$ for brevity. Further, $\hat{\mathbf{x}}$ is uniformly sampled from the straight line between a pair of points sampled from G and the corresponding NDCT images.

4) **Structural loss**: Medical images have strong 3D image correlations; their voxels demonstrate strong inter-dependencies which carry diagnostic information. Structural similarity index (SSIM) [44] and Multi-scale structural similarity index (MS-SSIM) [46] are better perceptually motivated metrics than mean-based metrics [44] since SSIM and MS-SSIM quantify structure errors (difference) between reference images and input images, and take advantage of the characteristics of the human visual system (HVS). To measure the

structural and perceptual similarity between two images, the formula of SSIM [44] is expressed as:

$$SSIM(\mathbf{x}, \mathbf{z}) = \frac{2\mu_x\mu_z + C_1}{\mu_x^2 + \mu_z^2 + C_1} * \frac{2\sigma_{xz} + C_2}{\sigma_x^2 + \sigma_z^2 + C_2} \quad (6)$$

$$= l(\mathbf{x}, \mathbf{z}) * cs(\mathbf{x}, \mathbf{z}) \quad (7)$$

where C_1, C_2 are constants and $\mu_x, \mu_z, \sigma_x, \sigma_z, \sigma_{xz}$ denote local means, standard deviation and cross-covariance of the image pair (\mathbf{x}, \mathbf{z}) from G and the corresponding NDCT respectively. $l(\mathbf{x}, \mathbf{z}), cs(\mathbf{x}, \mathbf{z})$ are the first term and second factor we defined in Eqn. 6.

Multiscale SSIM provides more flexibility for better generalization than the single-scale method, including different resolutions and local distortions [46]. The formula for MS-SSIM [46] is expressed as:

$$MS_SSIM(\mathbf{x}, \mathbf{z}) = \prod_{j=1}^M SSIM(\mathbf{x}_j, \mathbf{z}_j) \quad (8)$$

where $\mathbf{x}_j, \mathbf{z}_j$ are the local image content at the j^{th} local window, and M is the scale weight of local windows in the image.

The formula for structural loss (SL) is expressed as:

$$L_{SL} = 1 - MS_SSIM(\mathbf{x}, \mathbf{z}) \quad (9)$$

Note that the loss can be easily back-propagated to update weights in the network since it can be differentiated [38].

5) **Objective Function**: As mentioned in recent works [33], [38], minimizing L_2 loss between the image pair from the generator and the real NDCT leads to over-smoothed contents. The adversarial loss in GAN may yield sharp images, but it does not exactly match the corresponding real NDCT images [33]. The perceptual loss computed by a VGG network [42] evaluates the perceptual differences between the generated images and the real NDCT images in a high-level feature space instead of the voxel space. However, since the VGG network is trained on a large dataset of natural images, not CT images, it may result in anatomical distortions. To truly tackle these issues, we propose to utilize different loss layers to derive clinically high image quality.

As revealed in [38], L_1 loss can deliver noise suppression and increase SNR. However, it blurs anatomical structures to some extent. In contrast, structural loss can encourage less smoothness compared with L_1 loss and keep high contrast resolution. To capture merits of both loss functions, the structural sensitive loss (SSL) is expressed as:

$$L_{SSL} = \tau \times L_{SL} + (1 - \tau) \times L_1 \quad (10)$$

where τ is the scale weight to control the balance between structure preservation in the first term (from Eq. 9) and noise suppression in the second term (from Eq. 4).

However, these two methods may inevitably lose some important diagnostic features so adversarial loss is incorporated in our work to maintain texture and structure features. In summary, the overall objective function of SMGAN is expressed as:

$$L_{obj} = L_{SSL} + \beta \times L_{adv} \quad (11)$$

where β is the regularization weight to counteract the degree of smoothness. In the last step of the network, we compared the difference between the output volumes and the label volumes, and then the error was back-propagated through the network [47].

III. EXPERIMENTS AND RESULTS

A. Experimental Datasets and Setup

To show the effectiveness of the proposed network in LDCT noise reduction, we use a real clinical dataset, published by Mayo Clinic for the 2016 *NIH-AAPM-Mayo Clinic Low Dose CT Grand Challenge* [48]. The Mayo dataset consists of 2,378 normal dose CT (NDCT) and low dose (quarter dose) CT (LDCT) images from 10 anonymous patients. The reconstruction interval and slice thickness in our dataset were 0.8mm and 1.0mm respectively.

For **limited data**, in practice, the denoising performance of DL-based methods depends on the size of the training datasets, so large-scale valid training datasets can improve the denoising performance. However, it is worth noting that the training image library may not contain many valid images. To enhance the performance of the network, the strategies which we utilize are as follows. First of all, in order to improve generalization performance of the network and avoid over-fitting, we adopt the famous "10-fold cross validation" strategy. The original dataset is partitioned into 10 equal size subsets. Then, a single subset is used in turn as the validation subset and the rest of the subsamples are utilized as training subsets. Moreover, considering the limited number of CT images, we propose to adopt the overlapping patches strategy because it can not only consider patch-wise spatial interconnections, but also significantly increase the size of the training patch dataset [49], [50].

For **data preprocessing**, first, we apply the overlapping strategy in cropping over 100,000 pairs of training and label patches and over 5,000 pairs for validation from remaining patient images with the same size of $80 \times 80 \times 11$. Then, the "10-fold cross validation" strategy is adopted. Next, the CT Hounsfield Unit (HU) scale is normalized to [0, 1] before the images are fed to the network.

For **qualitative comparison**, in order to fully validate the performance of our proposed methods (SMGAN-2D and SMGAN-3D), we compare with eight state-of-the-art denoising methods, including CNN-L2 (L_2 -net), CNN-L1 (L_1 -net), structural-loss net (SL-net), multi-scale structural-loss net (MSL-net), WGAN, BM3D [23], RED-CNN [31], and WGAN-VGG [33]. Among these existing denoising methods, BM3D is a classical image space denoising algorithm. WGAN-VGG represents a 2D perceptual-loss-based network and RED-CNN refers to a 2D pixel-wise network. Note that the parameter settings in these methods [23], [31], [33] are followed per the suggestions from the original papers.

For **quantitative comparison**, to evaluate the effectiveness of the proposed methods, three state-of-the-art metrics are chosen to perform image quality evaluation, including peak signal-to-noise ratio (PSNR), structural similarity index (SSIM) [46], and root-mean-square error (RMSE).

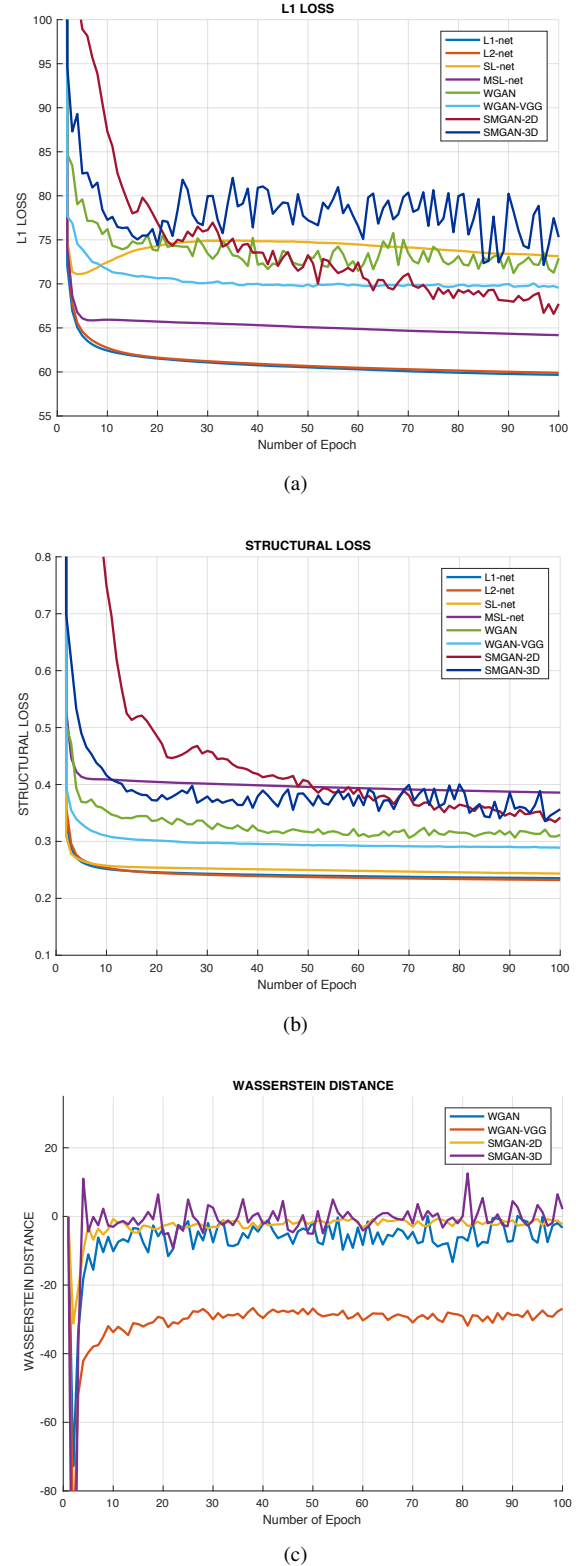


Fig. 2: Comparison among loss function value versus the number of epochs with respect to different algorithms. (a) L1 Loss convergence, (b) Structural Loss convergence, and (c) Wasserstein Distance convergence.

B. Parameter Selection

In our experiments, the Adam optimization algorithm is implemented in all our network training stages [51]. In the

training phase, the mini-batch size is 64. The hyperparameter λ for the balance between the Wasserstein distance and gradient penalty is set to be 10, with respect to the suggestions from the original paper [37]. The parameter β for the trade-off between adversarial loss and mixture loss is set as 10^{-3} . The parameter τ is set as 0.89. The slope of the leaky ReLU activation function is set as 0.2. The networks are implemented in the TensorFlow library [52] and an NVIDIA Titan Xp GPU was utilized in this study.

C. Network Convergence

To examine the robustness of different denoising algorithms, ten different methods corresponding to the L_1 loss (L_1), structural loss (SL), and Wasserstein distance are separately trained with same settings as SMGAN-3D. Note that the parameter settings of RED-CNN, WGAN-VGG, and BM3D from the original papers are followed [23], [31], [33]. In addition, the size of the input patches of the 2D network is 80×80 while our proposed 3D model uses training patches with the size of $80 \times 80 \times 11$. We calculate the averaged loss value achieved by different methods versus the number of epochs as the measure of convergence in Fig. 2. It is also worth noting that although these three reference loss functions are not implemented in one particular network during the same training phase, it is still meaningful to compare the convergence rates of different networks to study their performance.

In Fig. 2a and 2b, in terms of L_1 and SL, we observe that L_1 -net and L_2 -net achieve fastest convergence rate and have similar convergence trend in that all curves decrease initially and then smoothly converge, indicating that these mean-based algorithms both have fast convergence rate. Fig. 2a shows that they both converge around the 6th epoch. In contrast, in Fig. 2b, there are obvious differences between SL-based and mean-based methods. We can see that the convergence curve of the SL-net decreases initially and then slightly rises around the 4th epoch as shown in Fig. 2a. MSL-net also shows a small increase like SL-net in terms of L_1 . This observation indicates that SL-based and mean-based methods have different emphasis on minimizing perceptually motivated similarity between real NDCT images and generated NDCT images. As for WGAN-based methods, it can be clearly observed that the curves for WGAN, WGAN-VGG, SMGAN-2D, and SMGAN-3D slightly oscillate in the convergence process after approximately the 5th epoch in Fig. 2a and 2b. The reason for such oscillatory behaviors is as follows: G attempts to mimic the real NDCT distribution while D aims to differentiate between the real NDCT distribution and the denoised LDCT distribution. Since GAN's intrinsic nature is a two-player game, the distributions of G and D are constantly changing and this leads to the oscillatory behavior when converging to their optimal status.

As observed in Fig. 2c, we can evaluate the convergence performance of WGAN by comparing Wasserstein distance. It can be seen that our proposed SMGAN-2D has the mildest oscillatory behavior compared with the other three models and reaches a stable state after the 13th epoch. Moreover, the SMGAN-3D oscillates in a relatively large range in the

training process. This is because our proposed SMGAN-3D considers 3D structural information which results in a relatively larger vibrating amplitude in the training process. However, the curve still oscillates close to the x-axis, indicating SMGAN-3D's robustness in minimizing the Wasserstein distance between the generated samples and real samples. We hypothesize that such behavior may be related to their convexity properties.

The results imply that our proposed methods SMGAN-2D and SMGAN-3D achieve relatively fast convergence speed among different denoising networks as illustrated in Fig. 2a.

D. Denoising Performance

To demonstrate the effectiveness of the proposed network, we perform the qualitative comparisons over two representative abdominal images presented in Fig. 3 and Fig. 5. For better evaluations of the image quality with different denoising models, zoomed regions-of-interest (ROIs) are marked by red rectangles and shown in Fig. 4 and Fig. 6 respectively. Note that all results of different denoising models focus on two aspects: content restoration and noise-reduction. All CT images in axial view are displayed in the angiography window [-160, 240]HU.

The real NDCT images and corresponding LDCT images are presented in Figs. 3a and 3b. As observed, there are obvious distinctions between ground truth (NDCT) images and LDCT images. Fig. 3a shows the lesions of metastasis and Fig. 5a presents lesions of focal fatty sparing/focal fat. From Figs. 4a and 6a, these lesions can be clearly observed in NDCT images; in contrast, from Figs. 4b and 6b, it can be seen that the original LDCT image is noisy, and lacks structural features for task-based clinical diagnosis. All adopted denoising models suppress noise to some extent.

1) Comparison with CNN-based denoising methods: To study the robustness of the adversarial learning framework in SMGAN-3D, we compare SMGAN-3D with the CNN-based methods, including CNN-L2, CNN-L1, RED-CNN [31], SL-net and MSL-net. It is worth noting that CNN-L2, CNN-L1, and RED-CNN are mean-based denoising methods, and SL-net and MSL-net are SL-based denoising methods. All of the methods greatly reduce the noise compared with LDCT images. Our proposed method preserves more structural details, thereby yielding better image quality, compared with the other five methods.

Mean-based methods can effectively reduce noise, but the side effect is impaired image contents. In Fig. 3c, L_2 -net greatly suppresses the noise, but blurs some crucial structural information in the porta hepatis region. Meanwhile, some waxy artifacts can still be clearly observed in Fig. 6c. L_2 -net does not produce good visual quality because it assumes that the noise is independent of local characteristics of the images. Even though it retains high SNR, its results are not clinically preferable. Compared with L_2 -net, in Figs. 3d and 5d, it can be clearly seen that L_1 -net encourages less blurring and preserves more structure information. However, as observed in Fig. 4d, it still over-smooths some anatomical details. Meanwhile, in Fig. 6d, we can see that there are some

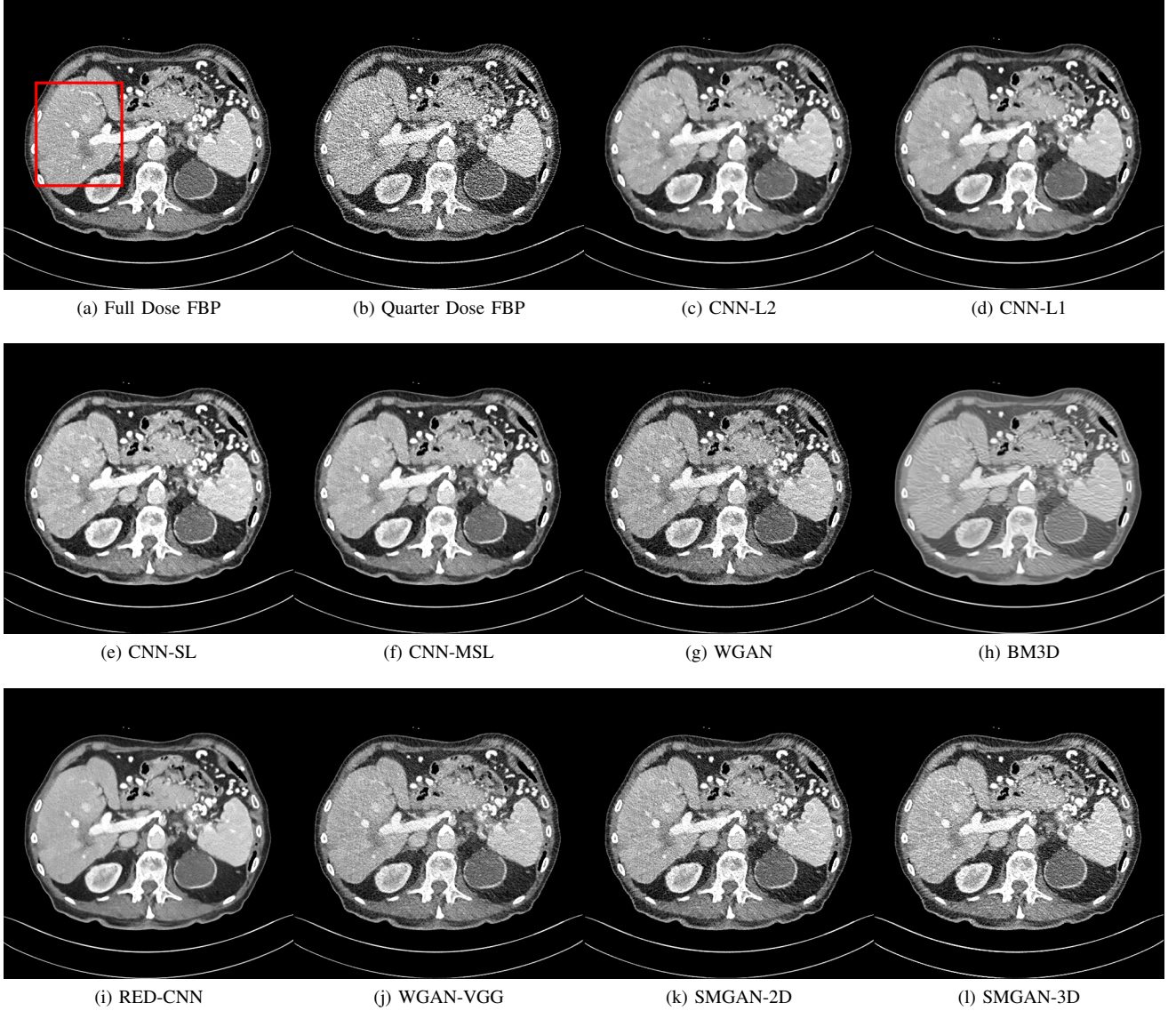


Fig. 3: Results from abdomen CT images.(a) NDCT, (b) LDCT, (c) CNN-L2, (d) CNN-L1, (e) SL-net, (f) MSL-net, (g) WGAN (h) BM3D, (i) RED-CNN, (j) WGAN-VGG, (k) SMGAN-2D, and (l) SMGAN-3D. The red rectangle indicates the region zoomed in Fig. 4. The display window is $[-160, 240]$ HU.

blocky effects marked by the blue arrow. The results obtained by RED-CNN [31] deliver high SNR but blur the vessel details as shown in Figs. 4i and 6i.

For SL-based methods, as observed in Figs. 3e and 5e, SL-net generates images with higher contrast resolution and preserves texture of real NDCT images better than L_2 -net and L_1 -net. However, 4e and 6e show that SL-net does not preserve the structural features well, and there still remain small streak artifacts. Subsequently, in Figs. 4e and 4f, SL-net and MSL-net have low frequency image intensity variance because SSIM/MS-SSIM is insensitive to uniform biases [44], [46]; on the other hand, L_1 -net preserves the overall image intensity, but it does not preserve high contrast resolution as SL-net and MSL-net do.

Overall, the observations above support the following statements. First, although the voxel-wise methods show good

noise-reduction properties, to some extent they blur the contents and lead to the loss of structural details because they optimize the results in the voxel-wise manner. Second, SL-based methods better preserve texture than mean-based methods, but they cannot preserve overall image intensity. Third, the results yielded by the proposed SMGAN-3D demonstrate the benefits of the combination of two loss functions and the importance of the adversarial training [36], [37].

2) **Comparison with WGAN-based denoising methods:** To evaluate the effectiveness of our proposed objective function, we compare our method with WGAN-based networks, including WGAN and WGAN-VGG. Considering the importance of clinical image quality and specific structural features to medical diagnosis, we adopt the adversarial learning method [36], [37] in our experiments because WGAN could help to capture more structural information. Nevertheless, based on our prior

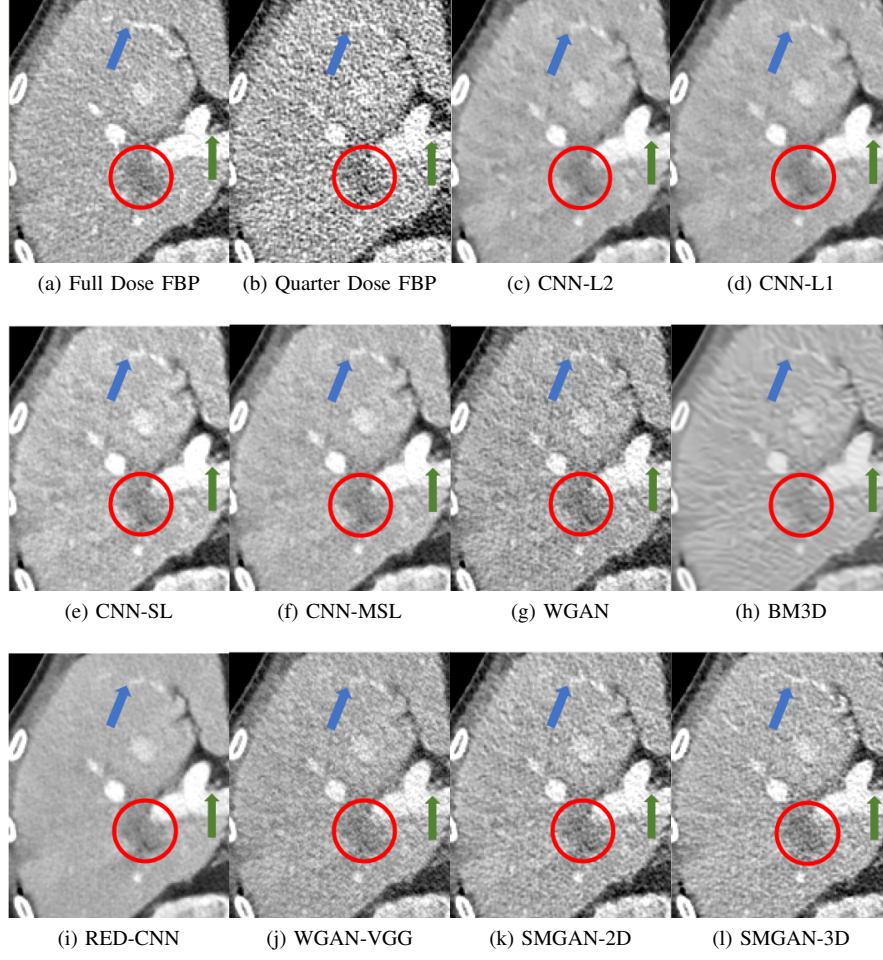


Fig. 4: Zoomed parts of the region of interest (ROIs) marked by the red rectangle in Fig. 3. (a) NDCT, (b) LDCT, (c) CNN-L2, (d) CNN-L1, (e) SL-net, (f) MSL-net, (g) WGAN, (h) BM3D, (i) RED-CNN, (j) WGAN-VGG, (k) SMGAN-2D and (l) SMGAN-3D. The red circle indicates the metastasis and the green and blue arrows indicate two subtle structure parts. The display window is $[-160, 240]\text{HU}$.

experience, only utilizing WGAN alone may yield stronger noise than other selected approaches, because it only maps the data distribution from LDCT to NDCT without consideration of local voxel and structural correlations. The observations demonstrate that the noise texture is coarse in the images, as shown in Fig. 4 and Fig. 6, which support our prior estimations.

Further, the images of WGAN-VGG [33], as shown in Fig. 3j, exhibit better visual quality with respect to more details and share similar structural details with NDCT images with respect to human perceptual evaluations. However, Figs. 4j (marked by red circle) and 6j (marked by green circle) suggest that it may severely distort the original structural information. A possible reason is that the VGG network [42] is a pre-trained deep CNN network based on natural images, and the structure information and contents of natural images are different from medical images.

Compared with WGAN and WGAN-VGG, our proposed SMGAN-3D, as shown in Figs. 4l (marked by red circle) and 6l (marked by green circle), can more clearly visualize

the metastasis and has better preservation of the portal vein.

The experimental results demonstrate that our proposed objective function is essential to capture more accurate anatomical details.

3) **Comparison with Image space denoising:** To validate the robustness of DL-based method, we compare our method with the image space denoising method. Figs. 4h and 6h show that BM3D blurs the low-contrast lesion marked by red circle and smooths specific features marked by blue arrow. In contrast, SMGAN-3D exhibits better contrast in the low-contrast lesion and yields much sharper features as shown in Figs. 4l and 6h.

4) **Comparison with 2D-based SMGAN network:** In order to evaluate the impact of 3D structure information, we compare SMGAN-3D with SMGAN-2D. As shown in Fig. 4l, our proposed SMGAN-3D generates the results with better subtle structural details than SMGAN-2D and enjoys much closer statistical noise properties to the corresponding NDCT images. The reasons why SMGAN-3D outperforms SMGAN-2D are follows. First, SMGAN-3D incorporates 3D structural

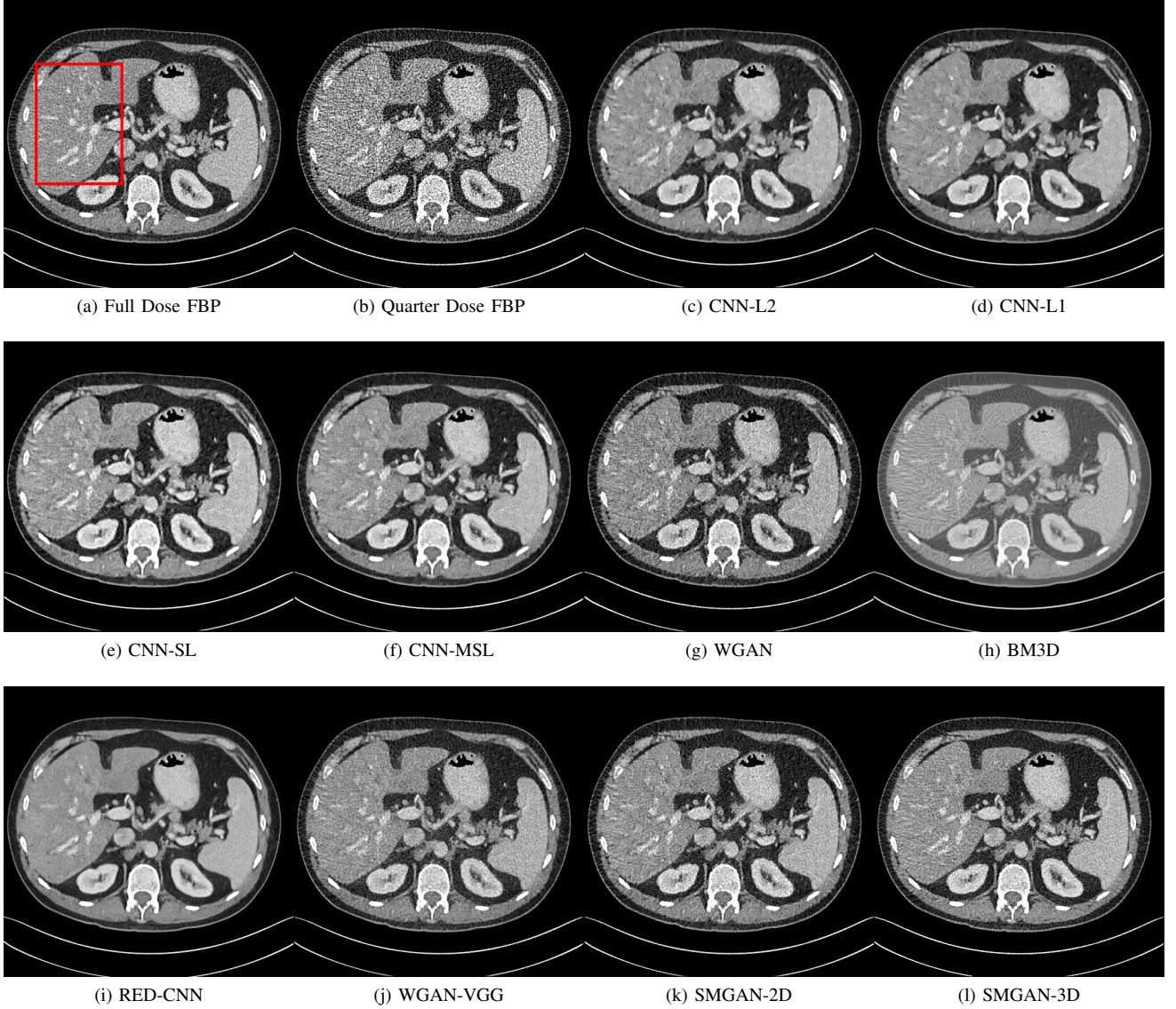


Fig. 5: Results from abdomen CT images. (a) NDCT, (b) LDCT, (c) CNN-L2, (d) CNN-L1, (e) SL-net, (f) MSL-net, (g) WGAN (h) BM3D, (i) RED-CNN, (j) WGAN-VGG, (k) SMGAN-2D, and (l) SMGAN-3D. The red rectangle indicates the region zoomed in Fig. 6. This display window is $[-160, 240]$ HU.

information to improve image quality. Second, SMGAN-2D takes input slice by slice, thus potentially leading to the loss of spatial correlation between adjacent slices.

In summary, we compared our proposed methods with existing methods, and it can be clearly observed that SMGAN-3D achieves robust performance in noise suppression, artifact removal, and capturing texture information. Note that we recommend the reader to see ROIs (in Fig. 4 and 6) or zoom in to better evaluate our results.

E. Quantitative analysis

Here, we first discuss the quantitative analysis with respect to three selected metrics (PNSR, SSIM, and RMSE). Then, we investigate the statistical properties of the denoised images to study the performance of each noise-reduction algorithm.

Next, we perform a blind reader study with three radiologists on 10 groups of images. Note that quantitative full-size measurements have been listed in Table I and image quality assessments of ROIs are drawn in Fig. 7. The gold-standard NDCT images are chosen as reference.

1) Image quality analysis: As shown in Table I, RED-CNN scores the highest PSNR and RMSE, and ranks second place in SSIM. Since the properties of PSNR and RMSE are regression to the mean, it is expected that RED-CNN, a mean-based regression optimization, has better performance than other feature-based models. For SL-net and MSL-net, it is not surprising that both models achieve the highest scores due to the adoption of structural similarity loss. However, a good score measured by image quality metrics does not ensure the preservation of high-level feature information and structural details, and this explains why RED-CNN can have the best

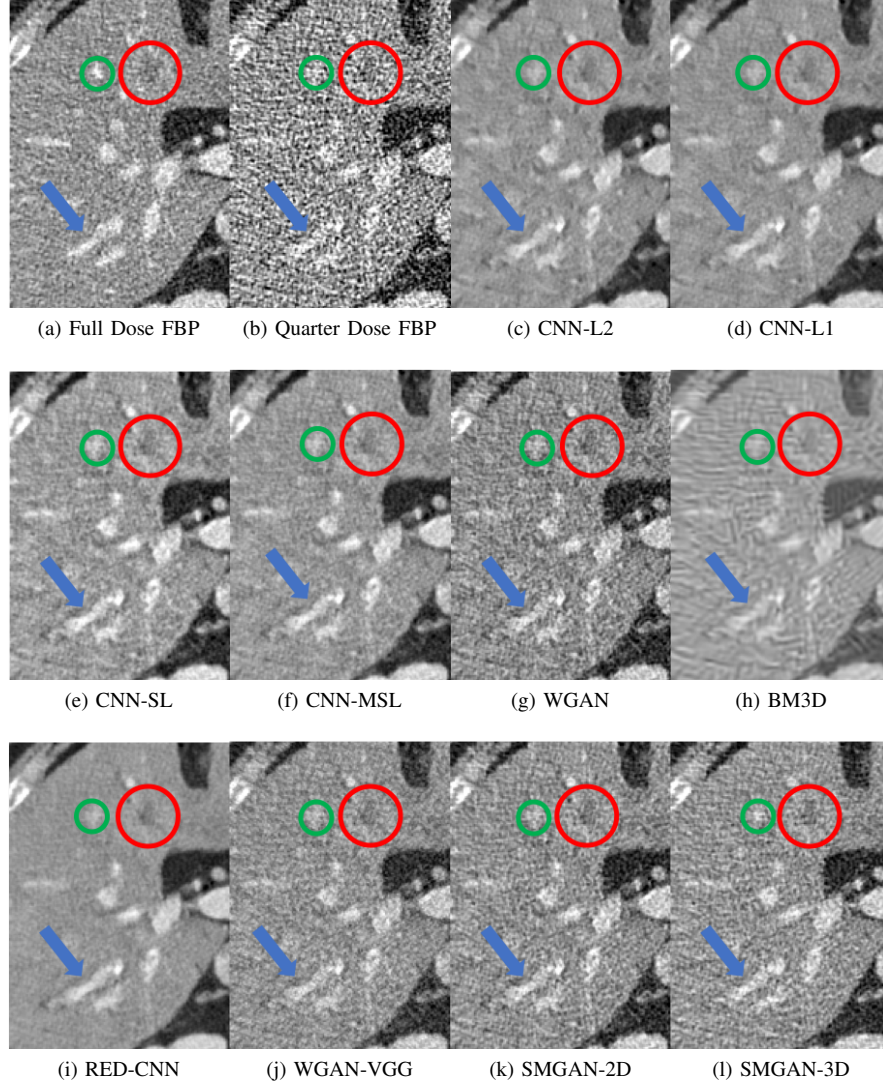


Fig. 6: Zoomed parts of the region of interest(ROIs) marked by the red rectangle in Fig. 5. (a) NDCT, (b) LDCT, (c) CNN-L2, (d) CNN-L1, (e) SL-net, (f) MSL-net, (g) WGAN, (h) BM3D, (i) RED-CNN, (j) WGAN-VGG, (k) SMGAN-2D and (l) SMGAN-3D. The dash circle indicates the metastasis and the green and blue arrows indicates two subtle structure parts. The display window is $[-160, 240]$ HU.

PSNR and RMSE despite over-smoothing the content.

Although mean-based approaches, such as L_1 -net, L_2 -net, enjoy high metric scores, they may over-smooth the overall image contents and lose feature characteristics, which do not satisfy our HVS requirements because this kind of regression methods favors the regression toward the mean. Meanwhile, WGAN-VGG satisfies HVS requirements, but gets the lowest scores in the three selected metrics. The reason for the lowest scores is that WGAN-VGG may suffers a few unknown subtle structural information or noise features, which may severely affect the accuracy of medical diagnosis. The proposed SMGAN-2D outperforms the feature-based method WGAN-VGG with reference to the three metrics, illustrating the robust denoising capability of the proposed loss layer. Compared with the SMGAN-2D model, SMGAN-3D achieves higher scores in PSNR and SSIM since it incorporates 3D

spatial information. To further validate the performance of each denoising model with respect to clinically significant local interested details, we perform the quantitative analysis over ROIs. The summary of the quantitative results from ROIs is shown in Fig. 7. It is worth noting that the quantitative results of ROIs follow a similar trend to that of the full-size images.

2) **Statistical properties analysis:** To quantitatively evaluate the statistical properties of processed images by different denoising models, we calculate the mean CT number (Hounsfield Units) and standard deviations (SDs) of ROIs, as shown in Table II. It is worth noting that how close the mean and SD value are represents the robustness of the denoising model to the reference (NDCT) images. As shown in Table II, L_1 -net, L_2 -net, SL-net, MSL-net, BM3D, RED-CNN, and WGAN-VGG generate much smaller SDs with respect to

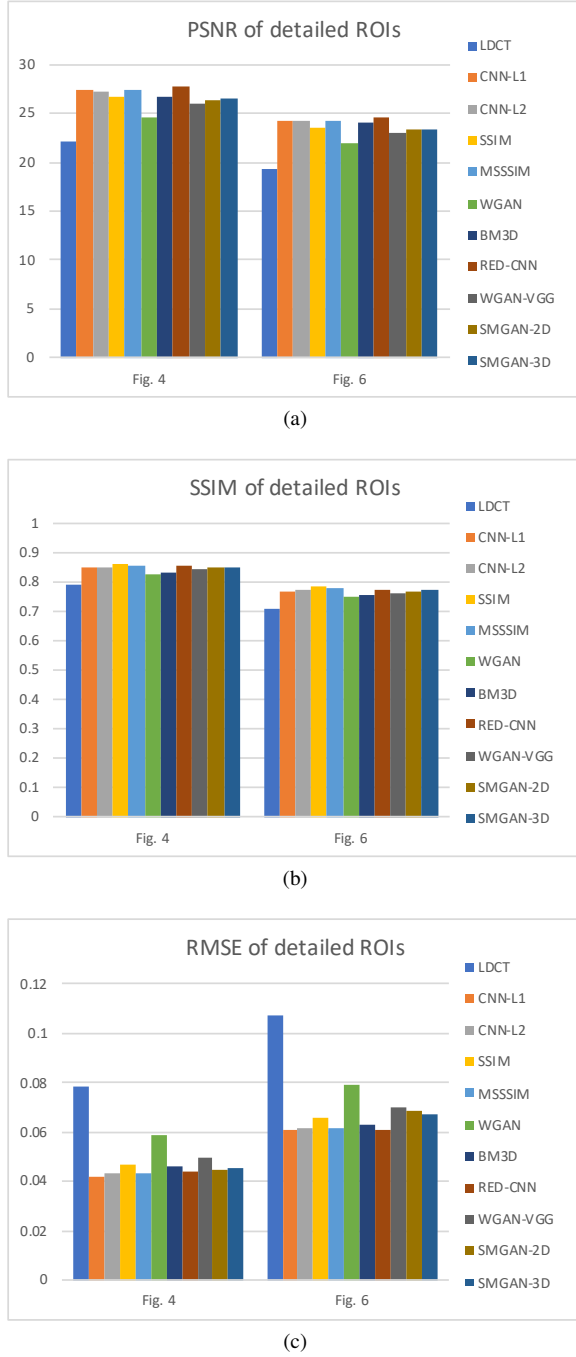


Fig. 7: Performance comparison of LDCT and ten algorithms for the ROIs marked by red rectangles in Fig. 3a and Fig. 5a.

NDCT images. This demonstrates that there are blocky and over-smoothing effects in the images which match our visual inspections. Specifically, for Fig. 6, the absolute difference in SDs between BM3D and NDCT is the largest among all of the denoising models, which indicates that BM3D has the most noticeable blurring effects. The standard deviation of BM3D supports our visual observations as shown in Figs. 4 and 6. The mean value of WGAN, WGAN-VGG, and SMGAN-2D deviated most from that of the NDCT image in Fig. 4. This indicates that WGAN, WGAN-VGG, and SMGAN-2D effectively reduce the noise level but compromise significant

TABLE I: Quantitative results associated with different approaches in Figs. 3 and 5.

	Fig. 3			Fig. 5		
	PSNR	SSIM	RMSE	PSNR	SSIM	RMSE
LDCT	22.818	0.761	0.0723	21.558	0.659	0.0836
CNN-L1	27.791	0.822	0.0408	26.794	0.738	0.0457
CNN-L2	27.592	0.819	0.0418	26.630	0.736	0.0466
SL-net	26.864	0.831	0.0453	25.943	0.745	0.0504
MSL-net	27.667	0.831	0.0414	26.685	0.744	0.0469
WGAN	25.727	0.801	0.0517	24.655	0.711	0.0585
BM3D	27.312	0.809	0.0431	26.525	0.728	0.0472
RED-CNN	28.279	0.825	0.0385	27.243	0.743	0.0444
WGAN-VGG	26.464	0.811	0.0475	25.300	0.722	0.0543
SMGAN-2D	26.627	0.821	0.0466	25.507	0.732	0.0530
SMGAN-3D	26.569	0.824	0.0473	25.372	0.739	0.0538

TABLE II: Statistical properties of the images in Fig. 4 and Fig. 6. These are the ROIs indicated by red rectangles in Figs. 3 and 5.

	Fig. 4		Fig. 6	
	Mean	SD	Mean	SD
NDCT	115.282	45.946	56.903	58.512
LDCT	114.955	74.299	57.228	85.854
CNN-L1	115.809	28.532	57.709	42.315
CNN-L2	117.191	29.933	58.956	43.411
SL-net	131.333	35.844	68.471	50.789
MSL-net	118.395	32.548	63.271	46.979
WGAN	105.461	42.659	48.432	54.306
BM3D	114.058	31.515	25.649	69.411
RED-CNN	116.642	27.194	57.985	42.048
WGAN-VGG	108.229	36.721	54.450	48.660
SMGAN-2D	108.758	40.948	51.243	53.065
SMGAN-3D	115.569	43.654	54.356	56.552

content information. Nevertheless, the SD value of SMGAN-2D is close to that of NDCT, which indicates that it supports HVS requirements. From the quantitative analysis in Table II, it can be observed that our proposed SMGAN-3D achieves the best match to the NDCT images out of all other methods. Therefore, SMGAN-3D is a highly competitive denoising model for clinical use.

3) **Visual assessments:** To truly validate clinical image quality of processed results, we performed a visual assessment with three radiologists on 10 groups of images. Each group includes an original LDCT image with lesions, the corresponding reference NDCT image, and the processed images by different denoising methods. NDCT, considered as the gold-standard, is the only labeled image in each group. All other images are evaluated on sharpness, noise suppression, diagnostic acceptability, and contrast retention using a five-point scale (5 = excellent and 1 = unacceptable). We invited three radiologists who have 12 years and 24 years clinical diagnosis experience respectively to join our study. Note that these results are evaluated independently and the overall image quality score for each method was computed by averaging scores from the four evaluation criteria. For different methods, the final score is formulated as mean \pm SD (average score of

TABLE III: Visual assessments by three radiologist readers.

	Sharpness	Noise Suppression	Diagnostic Acceptability	Contrast Retention	Overall Quality
LDCT	-	-	-	-	1.93
CNN-L1	2.80±0.81	3.30±0.71	2.70±0.78	2.75±0.77	2.89±0.77
CNN-L2	2.12±0.42	3.98±0.58	1.93±0.78	2.07±0.83	2.53±0.55
SL-net	2.95±0.86	3.15±0.65	2.70±0.71	2.80±0.81	2.90±0.76
MSL-net	3.01±0.94	3.16±0.57	2.87±0.83	2.84±0.69	2.97±0.76
WGAN	3.30±0.56	2.80±0.81	3.15±0.91	3.45±1.02	3.09±0.66
BM3D	2.21±1.08	3.29±0.80	2.21±0.86	2.29±0.88	2.50±0.91
RED-CNN	3.29±0.88	3.79±0.70	3.51±0.70	3.46±1.12	3.51±0.85
WGAN-VGG	3.35±0.91	3.50±1.07	3.35±0.91	3.45±1.02	3.41±0.94
SMGAN-2D	3.25±0.65	3.48±0.66	3.32±0.58	3.21±0.78	3.32±0.67
SMGAN-3D	3.56±0.73	3.59±0.68	3.58±0.46	3.61±1.02	3.59±0.72

three radiologists \pm standard deviation). The final quantitative results are listed in Table III.

As observed, the original LDCT result has the lowest scores because of their severe image quality degradation. All denoising models to some extent improve the scores in this case study. From Table III, we see that RED-CNN obtains the highest score in noise suppression. Compared to all other methods, our proposed SMGAN-3D scores best with respect to sharpness, diagnostic acceptability, and contrast retention. Furthermore, voxel-wise optimization has the least visually assessed image noise but obtains relatively low scores in sharpness and diagnostic acceptability, indicating a loss of image details. Last but not least, the SMGAN-3D model gets a higher overall image quality score than the 2D model, which indicates that a 3D model can enhance CT image denoising performance by incorporating spatial information from adjacent slices.

In brief, the visual assessment demonstrates that SMGAN-3D has powerful capabilities in noise reduction, subtle image structure and edge preservation, and artifact removal. Most importantly, it satisfies the HVS requirements as shown in Fig. 3 - 6.

F. Computational Cost

In CT reconstruction, there is a trade-off between the intensive computational cost and the image quality. To cope with such issues, the DL-based algorithm has great advantages in computation efficiency. Although the training of DL-based methods is time-consuming, it can rapidly perform the denoising tasks on reconstructed LDCT images after the training is completed. In our study, the proposed 2D method requires about 15 hours and the 3D model needs approximately 26 hours for training to converge. WGAN-VGG, which has the same number of layers, takes about 18 hours in the training phase. Compared with iterative reconstruction, any DL-based approach will require much less execution time, which facilitates workflow in the clinic. By experiments, the efficiency of our proposed model outperforms traditional reconstruction methods with respect to computation costs and processing time.

IV. DISCUSSIONS

We have presented a 3D CNN-based method for noise reduction in LDCT. As a follow-up to our previous work [33], a 3D convolutional neural network is utilized to improve the LDCT image quality by incorporating 3D volumetric feature representations. In addition, we have highlighted that the principal purpose of loss functions for clinical diagnosis is to preserve high-resolution features, subtle image texture and structure contents. Different from the state-of-the-art LDCT denoising method used in [32], an efficient structure-sensitive loss is carried out in a 3D manner to capture informative structural features and enhance the contrast resolution. Moreover, we have employed Wasserstein distance to stabilize training, thereby yielding a meaningful and smooth representation of the distance in-between. We have performed the quantitative analysis to evaluate the image quality. The quantitative assessments have demonstrated that SMGAN-3D can produce results with higher-level image quality for clinical usage compared with the existing denoising networks [30]–[33].

As discussed before, different focuses between visual evaluation and the image quality metric assessment have been extensively investigated. First, when training with only mean-based loss (L_1 -net, L_2 -net, RED-CNN), the results can achieve high scores in quantitative metrics and yield promising results with substantial noise reduction. Second, when training with the feature-based methods (WGAN-VGG), the results satisfy HVS requirements to produce better visualization since they preserve more structural details than mean-based methods. However, these methods suffer the potential risk of content distortion since a perceptual loss is computed based on a network [42] pre-trained on a natural image dataset. Third, practically and theoretically, even though adversarial learning methods can prevent smoothing in the image and capture structural characteristics, using them alone may result in severe loss of diagnostic information and lower SNR than that in the NDCT images. To capture the best characteristics of these loss function, we have proposed a progressive hybrid loss function to further improve image quality of the LDCT image.

Although our proposed network has achieved high-quality denoised LDCT images, there are still some limitations. First and foremost, the feature edges in the processed results may

still have blurring effects. Secondly, some structural variations between NDCT and LDCT did not perfectly match in each pixel. A better way to incorporate a dynamic routing model to enhance information correlation between NDCT and LDCT is to design a novel complex network to improve the transformation modeling capability, which is the work we have started.

V. CONCLUSION

In conclusion, we have proposed a novel 3D SMGAN DL-based denoising network as a generic noise-reduction model for clinical diagnosis. We have offered the thorough analysis on loss functions and focused on designing a novel loss function, which may have been overlooked in current denoising models for medical diagnosis. We have also utilized spatial information across multiple slices which can help overcome the limitations of voxel-wise regression and significantly improve diagnostic image quality. In the future, we will extend our model to other medical imaging modality restoration tasks, such as for magnetic resonance imaging (MRI), positron emission tomography (PET), and ultrasound. Moreover, we plan to incorporate more advanced denoising models such as the networks mentioned in [53]–[55] in LDCT reconstruction and fundamentally improve image quality.

ACKNOWLEDGMENT

The authors would like to thank NVIDIA Corporation for the donation of Titan Xp GPU utilized for this study. The authors are also grateful for inspirational discussions with Dr. Mats Persson (Stanford University).

REFERENCES

- [1] D. J. Brenner and E. J. Hall, "Computed tomography - an increasing source of radiation exposure," *New Eng. J. Med.*, vol. 357, no. 22, pp. 2277–2284, 2007.
- [2] A. B. de González, M. Mahesh, K.-P. Kim, M. Bhargavan, R. Lewis, F. Mettler, and C. Land, "Projected cancer risks from computed tomographic scans performed in the united states in 2007," *Arch. Intern. Med.*, vol. 169, no. 22, pp. 2071–2077, 2009.
- [3] D. A. Schauer and O. W. Linton, "National council on radiation protection and measurements report shows substantial medical exposure increase," pp. 293–296, 2009.
- [4] J. Wang, H. Lu, T. Li, and Z. Liang, "Sinogram noise reduction for low-dose CT by statistics-based nonlinear filters," in *Proc. of SPIE Vol.*, vol. 5747, 2005, p. 2059.
- [5] J. Wang, T. Li, H. Lu, and Z. Liang, "Penalized weighted least-squares approach to sinogram noise reduction and image reconstruction for low-dose X-ray computed tomography," *IEEE Trans. Med. Imaging*, vol. 25, no. 10, pp. 1272–1283, 2006.
- [6] M. Balda, J. Hornegger, and B. Heismann, "Ray contribution masks for structure adaptive sinogram filtering," *IEEE Trans. Med. Imaging*, vol. 31, no. 6, pp. 1228–1239, 2012.
- [7] A. Manduca, L. Yu, J. D. Trzasko, N. Khaylova, J. M. Kofler, C. M. McCollough, and J. G. Fletcher, "Projection space denoising with bilateral filtering and CT noise modeling for dose reduction in CT," *Med. Phys.*, vol. 36, no. 11, pp. 4911–4919, 2009.
- [8] G.-Z. Yang, P. Burger, D. N. Firmin, and S. Underwood, "Structure adaptive anisotropic image filtering," *Proc. IEEE Int. Conf. Image Process. Applicat.*, vol. 14, no. 2, pp. 135–145, 1996.
- [9] E. Y. Sidky, Y. Duchin, X. Pan, and C. Ullberg, "A constrained, total-variation minimization algorithm for low-intensity x-ray ct," *Med. Phys.*, vol. 38, no. S1, 2011.
- [10] B. De Man and S. Basu, "Distance-driven projection and backprojection in three dimensions," *Phys. Med. Biol.*, vol. 49, no. 11, p. 2463, 2004.
- [11] B. R. Whiting, P. Massoumzadeh, O. A. Earl, J. A. O'Sullivan, D. L. Snyder, and J. F. Williamson, "Properties of preprocessed sinogram data in x-ray computed tomography," *Med. Phys.*, vol. 33, no. 9, pp. 3290–3303, 2006.
- [12] I. A. Elbakri and J. A. Fessler, "Statistical image reconstruction for polychromatic X-ray computed tomography," *IEEE Trans. Med. Imaging*, vol. 21, no. 2, pp. 89–99, 2002.
- [13] Z. Tian, X. Jia, K. Yuan, T. Pan, and S. B. Jiang, "Low-dose CT reconstruction via edge-preserving total variation regularization," *Phys. Med. Biol.*, vol. 56, no. 18, p. 5949, 2011.
- [14] Y. Liu, J. Ma, Y. Fan, and Z. Liang, "Adaptive-weighted total variation minimization for sparse data toward low-dose x-ray computed tomography image reconstruction," *Phys. Med. Biol.*, vol. 57, no. 23, p. 7923, 2012.
- [15] Q. Xu, H. Yu, X. Mou, L. Zhang, J. Hsieh, and G. Wang, "Low-dose X-ray CT reconstruction via dictionary learning," *IEEE Trans. Med. Imaging*, vol. 31, no. 9, pp. 1682–1697, 2012.
- [16] Y. Zhang, X. Mou, G. Wang, and H. Yu, "Tensor-based dictionary learning for spectral CT reconstruction," *IEEE Trans. Med. Imaging*, vol. 36, no. 1, pp. 142–154, 2017.
- [17] E. Y. Sidky and X. Pan, "Image reconstruction in circular cone-beam computed tomography by constrained, total-variation minimization," *Phys. Med. Biol.*, vol. 53, no. 17, p. 4777, 2008.
- [18] Y. Chen, X. Yin, L. Shi, H. Shu, L. Luo, J.-L. Coatrieux, and C. Toumoulin, "Improving abdomen tumor low-dose CT images using a fast dictionary learning based processing," *Phys. Med. Biol.*, vol. 58, no. 16, p. 5803, 2013.
- [19] J. Ma, J. Huang, Q. Feng, H. Zhang, H. Lu, Z. Liang, and W. Chen, "Low-dose computed tomography image restoration using previous normal-dose scan," *Med. Phys.*, vol. 38, no. 10, pp. 5713–5731, 2011.
- [20] Z. Li, L. Yu, J. D. Trzasko, D. S. Lake, D. J. Blezek, J. G. Fletcher, C. H. McCollough, and A. Manduca, "Adaptive nonlocal means filtering based on local noise level for CT denoising," *Med. Phys.*, vol. 41, no. 1, 2014.
- [21] A. Buades, B. Coll, and J.-M. Morel, "A review of image denoising algorithms, with a new one," *Multiscale Model. Simul.*, vol. 4, no. 2, pp. 490–530, 2005.
- [22] A. Cheddad, C. Svensson, J. Sharpe, F. Georgsson, and U. Ahlgren, "Image processing assisted algorithms for optical projection tomography," *IEEE Trans. Med. Imaging*, vol. 31, no. 1, pp. 1–15, 2012.
- [23] P. F. Feruglio, C. Vinegoni, J. Gros, A. Sbarbati, and R. Weissleder, "Block matching 3D random noise filtering for absorption optical projection tomography," *Phys. Med. Biol.*, vol. 55, no. 18, p. 5401, 2010.
- [24] G. Wang, "A perspective on deep imaging," *IEEE Access*, vol. 4, pp. 8914–8924, 2016.
- [25] G. Wang, M. Kalra, and C. G. Orton, "Machine learning will transform radiology significantly within the next 5 years," *Med. Phys.*, vol. 44, no. 6, pp. 2041–2044, 2017.
- [26] W. Zhang, R. Li, H. Deng, L. Wang, W. Lin, S. Ji, and D. Shen, "Deep convolutional neural networks for multi-modality isointense infant brain image segmentation," *NeuroImage*, vol. 108, pp. 214–224, 2015.
- [27] S. Wang, M. Kim, G. Wu, and D. Shen, "Scalable high performance image registration framework by unsupervised deep feature representations learning," in *Deep Learning for Medical Image Analysis*. Elsevier, 2017, pp. 245–269.
- [28] X. Cao, J. Yang, Y. Gao, Q. Wang, and D. Shen, "Region-adaptive deformable registration of ct/mri pelvic images via learning-based image synthesis," *IEEE Trans. Image Process.*, 2018.
- [29] L. Cattell, G. Platsch, R. Pfeiffer, J. Declerck, J. A. Schnabel, C. Hutton, A. D. N. Initiative *et al.*, "Classification of amyloid status using machine learning with histograms of oriented 3d gradients," *NeuroImage: Clinical*, vol. 12, pp. 990–1003, 2016.
- [30] H. Chen, Y. Zhang, W. Zhang, P. Liao, K. Li, J. Zhou, and G. Wang, "Low-dose CT via convolutional neural network," *Biomed. Opt. Express*, vol. 8, no. 2, pp. 679–694, 2017.
- [31] H. Chen, Y. Zhang, M. K. Kalra, F. Lin, Y. Chen, P. Liao, J. Zhou, and G. Wang, "Low-dose CT with a residual encoder-decoder convolutional neural network," *IEEE Trans. Med. Imaging*, vol. 36, no. 12, pp. 2524–2535, 2017.
- [32] J. M. Wolterink, T. Leiner, M. A. Viergever, and I. Išgum, "Generative adversarial networks for noise reduction in low-dose CT," *IEEE Trans. Med. Imaging*, vol. 36, no. 12, pp. 2536–2545, 2017.
- [33] Q. Yang, P. Yan, Y. Zhang, H. Yu, Y. Shi, X. Mou, M. K. Kalra, and G. Wang, "Low dose CT image denoising using a generative adversarial network with wasserstein distance and perceptual loss," *arXiv preprint arXiv:1708.00961*, 2017.

- [34] E. Kang, J. Min, and J. C. Ye, "A deep convolutional neural network using directional wavelets for low-dose x-ray ct reconstruction," *arXiv preprint arXiv:1610.09736*, 2016.
- [35] H. Shan, Y. Zhang, Q. Yang, U. Kruger, W. Cong, and G. Wang, "3D convolutional encoder-decoder network for low-dose CT via transfer learning from a 2D trained network," *arXiv preprint arXiv:1802.05656*, 2018.
- [36] I. Goodfellow, J. Pouget-Abadie, M. Mirza, B. Xu, D. Warde-Farley, S. Ozair, A. Courville, and Y. Bengio, "Generative adversarial nets," in *Proc. Adv. Neural Inf. Process. Syst.*, 2014, pp. 2672–2680.
- [37] M. Arjovsky, S. Chintala, and L. Bottou, "Wasserstein GAN," *arXiv preprint arXiv:1701.07875*, 2017.
- [38] H. Zhao, O. Gallo, I. Frosio, and J. Kautz, "Loss functions for image restoration with neural networks," *IEEE Trans. Comput. Imaging*, vol. 3, no. 1, pp. 47–57, 2017.
- [39] L. Fu, T.-C. Lee, S. M. Kim, A. M. Alessio, P. E. Kinahan, Z. Chang, K. Sauer, M. K. Kalra, and B. De Man, "Comparison between pre-log and post-log statistical models in ultra-low-dose CT reconstruction," *IEEE Trans. Med. Imaging*, vol. 36, no. 3, pp. 707–720, 2017.
- [40] P. S. Calhoun, B. S. Kuszyk, D. G. Heath, J. C. Carley, and E. K. Fishman, "Three-dimensional volume rendering of spiral ct data: theory and method," *Radiographics*, vol. 19, no. 3, pp. 745–764, 1999.
- [41] V. Nair and G. E. Hinton, "Rectified linear units improve restricted boltzmann machines," in *Proc. 27th Int. Conf. Machine Learning*, 2010, pp. 807–814.
- [42] K. Simonyan and A. Zisserman, "Very deep convolutional networks for large-scale image recognition," *arXiv preprint arXiv:1409.1556*, 2014.
- [43] I. Gulrajani, F. Ahmed, M. Arjovsky, V. Dumoulin, and A. C. Courville, "Improved training of wasserstein gans," in *Proc. Advances Neural Information Processing Systems Conf.*, 2017, pp. 5769–5779.
- [44] Z. Wang, A. C. Bovik, H. R. Sheikh, and E. P. Simoncelli, "Image quality assessment: from error visibility to structural similarity," *IEEE Trans. Image Process.*, vol. 13, no. 4, pp. 600–612, 2004.
- [45] Z. Wang and A. C. Bovik, "Mean squared error: Love it or leave it? a new look at signal fidelity measures," *IEEE Signal Process. Mag.*, vol. 26, no. 1, pp. 98–117, 2009.
- [46] Z. Wang, E. P. Simoncelli, and A. C. Bovik, "Multiscale structural similarity for image quality assessment," in *Proc. IEEE Asilomar Conf. Signals, Syst., Comput.*, vol. 2. Ieee, 2003, pp. 1398–1402.
- [47] Y. LeCun, L. Bottou, Y. Bengio, and P. Haffner, "Gradient-based learning applied to document recognition," *Proc. IEEE*, vol. 86, no. 11, pp. 2278–2324, 1998.
- [48] AAPM, "Low dose ct grand challenge," 2017. [Online]. Available: <http://www.aapm.org/GrandChallenge/LowDoseCT/#>
- [49] J. Xie, L. Xu, and E. Chen, "Image denoising and inpainting with deep neural networks," in *Proc. Adv. Neural Inf. Process. Syst.*, 2012, pp. 341–349.
- [50] C. Dong, C. C. Loy, K. He, and X. Tang, "Image super-resolution using deep convolutional networks," *IEEE Trans. Pattern Anal. Mach. Intell.*, vol. 38, no. 2, pp. 295–307, 2016.
- [51] D. P. Kingma and J. Ba, "Adam: A method for stochastic optimization," *arXiv preprint arXiv:1412.6980*, 2014.
- [52] M. Abadi, A. Agarwal, P. Barham, E. Brevdo, Z. Chen, C. Citro, G. S. Corrado, A. Davis, J. Dean, M. Devin *et al.*, "Tensorflow: Large-scale machine learning on heterogeneous distributed systems," *arXiv preprint arXiv:1603.04467*, 2016.
- [53] J. Dai, H. Qi, Y. Xiong, Y. Li, G. Zhang, H. Hu, and Y. Wei, "Deformable convolutional networks," *CoRR*, *abs/1703.06211*, vol. 1, no. 2, p. 3, 2017.
- [54] K. He, X. Zhang, S. Ren, and J. Sun, "Deep residual learning for image recognition," in *Proc. IEEE Conf. Comp. Vis. Patt. Recogn.*, 2016, pp. 770–778.
- [55] S. Sabour, N. Frosst, and G. E. Hinton, "Dynamic routing between capsules," in *Proc. Adv. Neural Inf. Process. Syst.*, 2017, pp. 3859–3869.